Holistic Mapping of Striatum Surfaces in the Laplace-Beltrami Embedding Space

Jin Kyu Gahm[(✉)] and Yonggang Shi

Laboratory of Neuro Imaging, USC Stevens Neuroimaging and Informatics Institute,
Keck School of Medicine, University of Southern California, Los Angeles, USA
jkgahm@loni.usc.edu

Abstract. In brain shape analysis, the striatum is typically divided into three parts: the caudate, putamen, and accumbens nuclei for its analysis. Recent connectivity and animal studies, however, indicate striatum-cortical inter-connections do not always follow such subdivisions. For the holistic mapping of striatum surfaces, conventional spherical registration techniques are not suitable due to the large metric distortions in spherical parameterization of striatal surfaces. To overcome this difficulty, we develop a novel striatal surface mapping method using our recently proposed Riemannian metric optimization techniques in the Laplace-Beltrami (LB) embedding space. For the robust resolution of sign ambiguities in the LB spectrum, we also devise novel anatomical contextual features to guide the surface mapping in the embedding space. In our experimental results, we compare with spherical registration tools from FreeSurfer and FSL to demonstrate that our novel method provides a superior solution to the striatal mapping problem. We also apply our method to map the striatal surfaces from 211 subjects of the Human Connectome Project (HCP), and use the surface maps to construct a cortical connectivity atlas. Our atlas results show that the striato-cortical connectivity is not distinctive according to traditional structural subdivision of the striatum, and further confirms the holistic approach for mapping striatal surfaces.

1 Introduction

Striatum is a critical sub-cortical structure that connects the cortex and other basal ganglia structures. It is an essential part of the cortico-striatal-thalamo-cortical (CSTC) network that regulates human emotion and behaviors [1]. With T1-weighted MRI, shape analysis has been applied to study morphometry changes of the striatum in neurological [2] and mental disorders [3] by dividing the striatum into three parts: the caudate, putamen, and accumbens nuclei. Recent connectivity research [4,5] and animal studies [6], however, indicate that
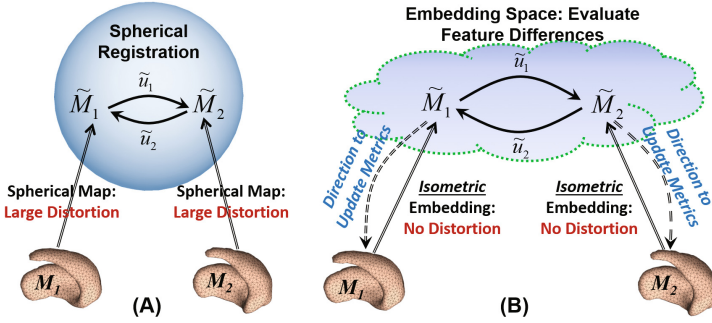
Fig. 1. A conceptual comparison of (A) the spherical registration method and (B) our metric optimization method in the Laplace-Beltrami embedding space for the mapping of two striatum surfaces M_1 and M_2. The fundamental advantage of the metric optimization framework is that there is no extra distortion induced by the parameterization process. All the metric changes are induced to match the two surfaces. On the other hand, the spherical mapping process introduces large metric distortions purely for the parameterization step, which can lead to large errors in the final maps.

striatum functions do not follow such subdivisions and it is more natural to map the striatum as a holistic structure. In this work, we follow this line of research in neuroscience and develop a novel striatum surface mapping method for studying its connectivity and function.

The novel surface mapping method we develop is based on Riemannian metric optimization on surfaces (RMOS) in the Laplace-Beltrami (LB) embedding space we recently proposed in [7]. As illustrated in Fig. 1, our metric optimization approach eliminates the large metric distortion during the parameterization step of conventional spherical registration methods [8–10]. This fundamental advantage stems from the isometry of the LB embedding [11]. This is especially important for mapping the striatum as a holistic surface because of its drastically different geometry as compared to the unit sphere. To drive the striatum surface mapping in the LB embedding space, we also develop novel anatomical contextual features using the relation of neighboring brain structures. This helps establish anatomically meaningful maps and remove sign ambiguity in the LB eigenfunctions, which is a critical problem in shape analysis using the LB spectrum [12,13]. In our experimental results, we compare our novel striatum mapping method with two spherical registration algorithms from FreeSurfer [8] and FSL [10], and apply it to a large-scale dataset from Human Connectome Project (HCP) [14] for the construction of a surface-based connectivity atlas of the striatum.

2   Methods

Striatal Surface Reconstruction. To perform striatal surface mapping, we first reconstruct a triangular mesh representation of the striatum in each

hemisphere of the human brain from T1-weighted MRI (Fig. 2). Because publicly available tools typically segment out the caudate, putamen, and accumbens nuclei of the striatum, we merge them into one mask and apply the surface reconstruction method in our MOCA software tool [15] on NITRC. This algorithm ensures all surfaces have genus-zero topology, and removes segmentation artifacts without volume shrinkage. Finally we decimate each mesh to 1000 vertices and 2994 edges for all mapping tasks.

Fig. 2. Surface representation of (A) subdivision of the striatum; (B) the whole striatum.
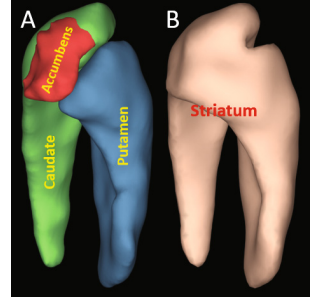
Metric Optimization in LB Embedding Space. Let $\mathcal{M}_1$ and $\mathcal{M}_2$ denote the mesh representation of two striatum surfaces, ξ_1^j and $\xi_2^j (j = 1, \cdots, L)$ denote the L features defined on the two surfaces to guide their mapping, and W_1 and W_2 denote their Riemannian metrics, i.e., the edge weights. Given the Riemannian metrics, we can compute the LB embeddings of $\mathcal{M}_i (i = 1, 2)$ as:

$$I_{\mathcal{M}_i}^{\Phi_i}(x) = (\frac{f_1^i(x)}{\sqrt{\lambda_1^i}}, \frac{f_2^i(x)}{\sqrt{\lambda_2^i}} \cdots , \frac{f_n^i(x)}{\sqrt{\lambda_n^i}}, \cdots) \quad \forall x \in \mathcal{M}_i, \tag{1}$$

where λ_n^i and f_n^i denote the n-th eigenvalue and eigenfunction of $\mathcal{M}_i$ [7]. To compute the surface maps $u_1 : \mathcal{M}_1 \to \mathcal{M}_2$ and $u_2 : \mathcal{M}_2 \to \mathcal{M}_1$, we will minimize an energy function via metric optimization as follows:

$$E(W_1, W_2, u_1, u_2) = \underbrace{\sum_{j=1}^{L} \left[\int_{\mathcal{M}_1} C_j \left(\xi_1^j, \xi_2^j \circ u_1 \right) d\mathcal{M}_1 + \int_{\mathcal{M}_2} C_j \left(\xi_2^j, \xi_1^j \circ u_2 \right) d\mathcal{M}_2 \right]}_{\text{Feature Term } E_F}$$
$$+ \underbrace{\gamma(\text{Reg}(W_1) + Reg(W_2))}_{\text{Regularization Term } E_R} \tag{2}$$

There are two terms in the energy function: feature term E_F, and regularization term E_R with the coefficient γ for the smoothness of the Riemannian metrics. The feature term measures the agreement of corresponding features. For the j-th feature, the cost function C_j measures the similarity of the same feature at the corresponding locations of the two surfaces induced by the surface maps u_1 and u_2. In this work, we define the cost function as the l_2 energy, but more general choices such as mutual information are also possible. The regularization energy is designed to avoid overly irregular distortion during the mapping process. In this work, we define E_R at each edge as the l_2 difference between its metric ratio and the mean value of its neighbors.

As shown in Fig. 3, there are three main steps in the energy minimization. Given the current metrics, we compute the LB eigen-system and construct their LB embeddings in Step 1. Also, the sign and order ambiguities in the eigenfunctions are resolved in this step by searching for the optimal embedding from possible combinations of the eigenfunctions. To better estimate the right combination, we compute the feature energy E_F in Eq. 2 with the nearest

Step 1: LB Embedding of $\mathcal{M}_1$ and $\mathcal{M}_2$
- Compute eigen-system with current metrics: W_1 and W_2
- Form the LB embedding for both surfaces after removing sign and order ambiguities: $I_{\mathcal{M}}^{\Phi}(x)$ in Eq. 1.

Step 2: Embedding Space: β-map Construction
- Initialize with the nearest point map
- Evolve the map in the tangent space:
$$\frac{\partial E_F}{\partial \tilde{u}_1^{\beta}} = -2 \sum_{j=1}^{L} \left(\xi_1^j - \xi_2^j \circ \tilde{u}_1^{\beta} \right) \nabla_{\widetilde{\mathcal{M}}_2} \xi_2^j(\tilde{u}_1^{\beta})$$
- Convert E_F into a distance energy $\widetilde{E}_F$

Step 3: Metric Optimization to Minimize $E = \widetilde{E}_F + \gamma E_R$
- Compute gradients of eigen-system w.r.t the metric
- Form gradients of the energy w.r.t. the metric
- Update metrics W_1 and W_2 with gradient projection

Fig. 3. The main algorithmic steps to compute the striatal surface maps.

point map for every possible combination of the eigenfunctions, and search for the optimal embedding only from the combinations for which the feature energy is sufficiently low (below the lower 10 percentile in this work). To link the mismatch of features with the metrics, we then compute the β-maps $\tilde{u}_i^{\beta}$ along the gradient descent direction of E_F and convert it into a distance energy $\tilde{E}_F$ in Step 2. This is a critical step as the distance energy in the embedding space is a function of the eigen-systems as defined in [13], so it allows the computation of the gradient of the final energy E with respect to the metrics. This information is sent back to the image space to update the metrics W_1 and W_2 in Step 3. After that, the three steps are repeated until convergence. The final maps are obtained via composition of the embeddings and the maps in the embedding space. Because both surfaces are treated equally in the RMOS framework, the maps are symmetric.

As shown in Fig. 1(B), this computational framework uses the high dimensional LB embedding space as a canonical space instead of the 2D sphere (Fig. 1(A)). The isometry of the LB embedding ensures that the numerical calculation we perform in the embedding space stays faithful to the original surfaces. The surface registration algorithm in the framework is also fundamentally different from conventional nonlinear mesh deformation on the sphere [8,9]. To calculate a general diffeomorphism between surfaces, iterative optimization of the metrics on mesh edges was conducted instead of deforming the meshes in the embedding space. This means that we only need to optimize a set of scalar functions on the surfaces without the need of worrying about numerical difficulties such as the flipping of triangles or self-intersection. This numerical advantage is from the theoretical guarantee that the LB embedding is fully determined by
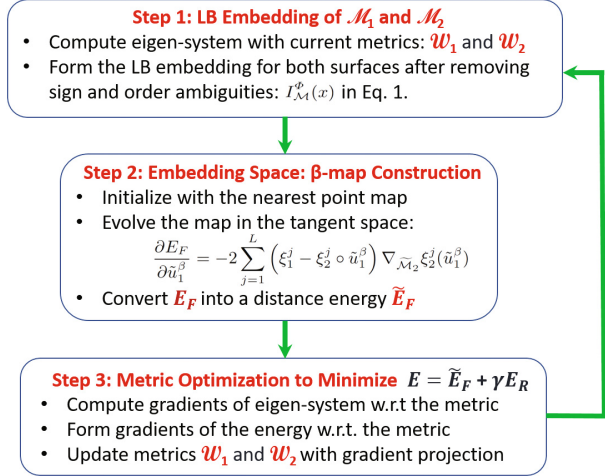
the Riemannian metric on the surfaces and the Riemannian metric can be fully determined by a diffeomorphism via the pullback metric.
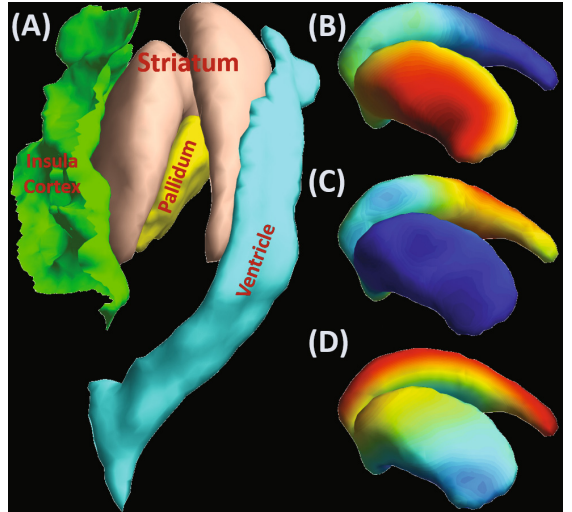
Anatomical Contextual Features for Striatal Surface Mapping. The metric optimization framework is flexible and can take general features to guide surface mapping in the LB embedding space. For the mapping of striatal surfaces, we will utilize contextual information for robustness. Compared with local features derived from curvatures, the context features provide a global characterization about "where to where" in the mapping process. Importantly, they also help resolve the sign ambiguity of the LB eigen-system by providing a unique description in different parts of a structure, especially when there exist some symmetries of the structure shape. Finally, the redundant characterizations from

Fig. 4. An illustration of Anatomical Neighbor Context (ANC). (A) a striatum surface and its neighboring structures used for defining the ANC. Normalized distance features to the ventricle, insula, and pallidum are shown in (B), (C), and (D), respectively.

all the features will increase robustness in mapping results.

For striatal surface mapping, we develop anatomical neighbor context (ANC) features that characterize the geometric relation between neighboring brain structures. At each vertex of a surface, a contextual feature will be represented as a vector. Let d_i $(i = 1, 2, \cdots, C)$ denote the l_2-distance transform of its i-th neighbor. For each vertex $V_j \in \mathcal{M}$, its ANC is defined as

$$ANC(V_j) = \left[\frac{d_1(V_j)}{\max\limits_{V_k \in \mathcal{M}} d_1(V_k)}, \frac{d_2(V_j)}{\max\limits_{V_k \in \mathcal{M}} d_2(V_k)}, \cdots, \frac{d_C(V_j)}{\max\limits_{V_k \in \mathcal{M}} d_C(V_k)} \right]. \qquad (3)$$

By normalizing each distance transform by its maximal value on the surface, we make the ANC feature invariant to scale differences. As an example, we show in Fig. 4 the ANC features for a striatal surface with respect to three neighbors: the lateral ventricle, insular cortex and pallidum. These features provide complementary information in different parts of the striatum. Taken together, they give a highly informative description about the corresponding locations across different subjects.

3   Results

Curvature-Driven Surface Mapping. As a first experiment, we demonstrate curvature-driven mapping between two left striatal surfaces shown in Fig. 5(A) and (B) using RMOS and spherical registration. The surfaces are colored by mean curvature (MC) that is normalized by surface volume for surface mapping. We computed the RMOS map with the maximum of 60 eigenfunctions, and the regularization coefficient of 0.1. For spherical registration, the two surfaces were first parameterized to the unit sphere (Fig. 5(E) and (F)) using SPHARM-MAT [16], with the maximum SPHARM degree of 6 and other recommended parameter settings. Then the source sphere was registered to the target sphere by matching the MC using FreeSurfer's mris_register [8] and FSL's msm [10] under the default parameter settings.
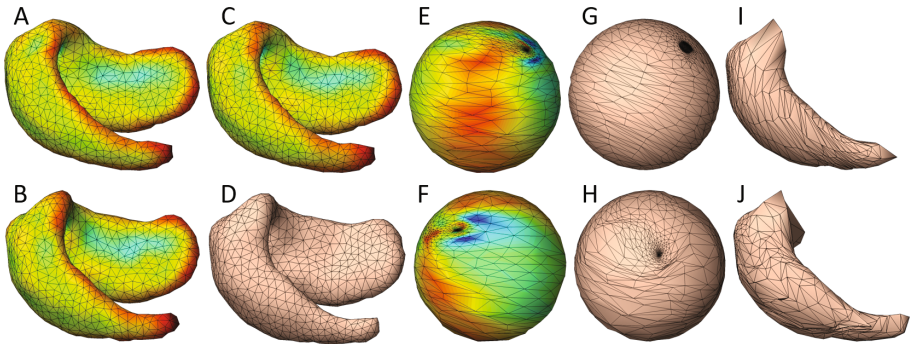
Fig. 5. Curvature-driven mapping between two left striatal surfaces. (A) The source and (B) target surfaces are colored by mean curvature (MC). Using the maps computed by MC-driven RMOS, we pull back the MC of the target surface onto the source surface (C), and project the source onto the target surface (D). The two striatal surfaces in (A, B) were parametrized to (E, F) the unit spheres (colored by MC in (A, B)) using SPHARM-MAT, (E) the source sphere was registered to (F) the target sphere using (G) FreeSurfer and (H) FSL. Projection of the source striatal surface in (A) to the target surface by the spherical map is shown in (I, J), respectively.

Large metric distortions were introduced in spherical parameterization as shown in Fig. 5(E) and (F), which led to significant errors in the subsequent spherical registration from the source to target sphere as shown in Fig. 5(G) and (H) by FreeSurfer and FSL, respectively. It is more obviously observed, in projection of the source to target striatal surface via the maps computed by spherical registration (Fig. 5(I) and (J)), that spherical mapping failed in the establishment of correspondences especially in the putamen part. This failure was consistently observed in spherical mapping of other striatal surfaces. With MC-driven RMOS, we can see in Fig. 5(C) and (D) that high quality surface maps have been achieved with little metric distortion.
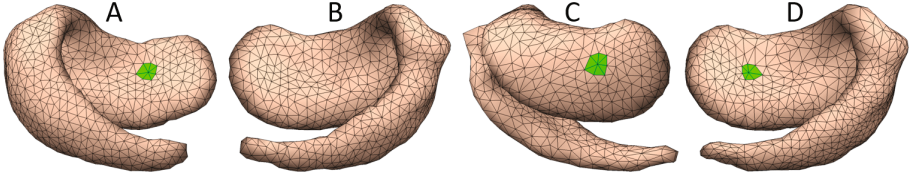
Fig. 6. RMOS mapping from (A) a left striatal surface to (B) a right striatal surface driven by (C) MC only and (D) ANC (with MC). (C) In projection of the left to right striatal surface by the map of MC-driven RMOS, the green patch on the left putamen in (A) was mapped onto the opposite side of the right putamen in (C). (D) ANC-driven RMOS correctly maps the patch onto the same side of the right putamen in (D). The surface views in (C) is opposite to (A, B, D) (lateral vs. medial views).

ANC-Driven RMOS Mapping. In this experiment, we demonstrate ANC-driven RMOS mapping between left and right striatal surfaces, which is more challenging because the symmetry between the left and right shapes makes it more difficult to resolve the sign ambiguity in the early mapping process. As shown in Fig. 6(C), MC-driven RMOS failed to establish anatomically correct correspondences (for example, the green patch on the putamen) for a pair of left and right striatal surfaces shown in Fig. 6(A) and (B). This is because MC did not provide a unique description in different parts of the striatum, especially in the putamen part. Using both the MC and ANC features developed in this work, we can see that RMOS is able to correctly map the corresponding anatomy (Fig. 6(D)).

Striatal Connectivity Atlas. In the final experiment, we constructed a surface-based connectivity atlas of the left striatum from 211 subjects of the Q1–Q3 release of HCP. We computed striatal connectivity using probabilistic tractography with fiber orientation distributions (FODs) reconstructed from the multi-shell diffusion MRI data [17]. We generated the connectivity maps to seven cortical regions: orbital-frontal (medial only), middle/inferior-frontal, superior-frontal, precentral, parietal, occipital, and temporal cortices [4] as done from the thalamus in [7].

For construction of the connectivity atlas, RMOS maps between one reference surface and the other 210 surfaces was computed using both the three ANC and MC features with the same RMOS parameters above. Then the connectivities on each surface were pulled back to the reference surface by the RMOS maps, and we have a vector of the 211 connectivities to each cortical region for every vertex on the reference surface. The probabilistic atlas of each cortical regions was defined as the number of the connectivities to the cortical region higher than 10% divided by the total number 211 for every vertex. Then we thresholded the probabilistic atlas at 25%, which are shown in Fig. 7(A). Finally, the labeled atlas was computed by assigning each vertex to the cortical region to which it had the highest probability of the connection.
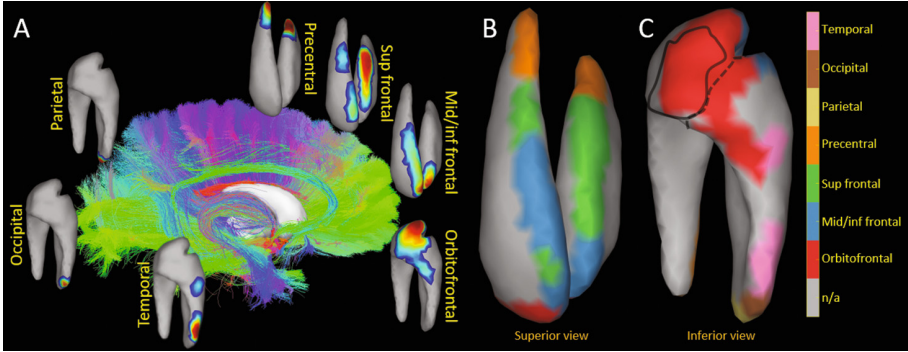
Fig. 7. Striato-cortical connectivity atlas of 211 subjects. From the connectivities on all the striatal surfaces projected to the reference surface with the RMOS maps, (A) a probabilistic atlas was computed and thresholded at 25% for each cortical region. The labeled atlas by the highest probability of connection is shown in (B) and (C). The accumbens boundary and the boundary between putamen and caudate are drawn on the surface in (C) as solid and dashed curves, respectively.

Each cortical region is topographically connected to adjacent areas on the striatal surface, but there is little connection at the lateral parts of the striatal surface as observed in tractography around the striatum (Fig. 7(A)). This is possibly due to the difficulty of current tractography techniques in detecting extremely short connections to neighboring cortices. More importantly, the striato-cortical connectivity patterns do not follow the conventional subdivison from the FSL segmentation tool. In particular, the striatal connection to the orbito-frontal cortex not only occupies the nucleus accumbens but also extends to the ventral part of the putamen/caudate as shown in Fig. 7(C).

4   Conclusion

In this paper, we developed a novel holistic mapping method for studying striatum structure and connectivity. Using the data from 211 HCP subjects, we constructed a tractography-based striato-cortical connectivity atlas. We successfully established the detailed correspondences across the striatal surfaces using RMOS driven by the novel ANC features. The projected connectivities to each cortical region by the RMOS maps are highly clustered on functional ROIs that do not follow the traditional structural subdivision of the striatum. For future work, with our high-quality surface maps of the striatum, we will build a striatal connectivity atlas using resting-state fMRI that provides more accurate functional connections.

References

1. Shepherd, G.: Corticostriatal connectivity and its role in disease. Nat. Rev. Neurosci. **14**, 278–291 (2013)
2. Muralidharan, P., Fishbaugh, J., Johnson, H.J., Durrleman, S., Paulsen, J.S., Gerig, G., Fletcher, P.T.: Diffeomorphic shape trajectories for improved longitudinal segmentation and statistics. In: Golland, P., Hata, N., Barillot, C., Hornegger, J., Howe, R. (eds.) MICCAI 2014. LNCS, vol. 8675, pp. 49–56. Springer, Cham (2014). doi:10.1007/978-3-319-10443-0_7
3. Mamah, D., Alpert, K.I., Barch, D.M., Csernansky, J.G., Wang, L.: Subcortical neuromorphometry in schizophrenia spectrum and bipolar disorders. NeuroImage Clin. **11**, 276–286 (2016)
4. Tziortzi, A.C., Haber, S.N., Searle, G.E., Tsoumpas, C., Long, C.J., Shotbolt, P., Douaud, G., Jbabdi, S., Behrens, T.E., Rabiner, E.A., et al.: Connectivity-based functional analysis of dopamine release in the striatum using diffusion-weighted MRI and positron emission tomography. Cereb. Cortex (2013). doi:10.1093/cercor/bhs397
5. Jaspers, E., Balsters, J.H., Kassraian Fard, P., Mantini, D., Wenderoth, N.: Corticostriatal connectivity fingerprints: probability maps based on resting-state functional connectivity. Hum. Brain Mapp. **38**, 1478–1491 (2016)
6. Burguière, E., Monteiro, P., Feng, G., Graybiel, A.M.: Optogenetic stimulation of lateral orbitofronto-striatal pathway suppresses compulsive behaviors. Science **340**(6137), 1243–1246 (2013)
7. Gahm, J.K., Shi, Y.: Riemannian metric optimization for connectivity-driven surface mapping. In: Ourselin, S., Joskowicz, L., Sabuncu, M.R., Unal, G., Wells, W. (eds.) MICCAI 2016. LNCS, vol. 9900, pp. 228–236. Springer, Cham (2016). doi:10.1007/978-3-319-46720-7_27
8. Fischl, B., Sereno, M.I., Dale, A.M.: Cortical surface-based analysis II: Inflation, flattening, and a surface-based coordinate system. NeuroImage **9**(2), 195–207 (1999)
9. Yeo, B., Sabuncu, M., Vercauteren, T., Ayache, N., Fischl, B., Golland, P.: Spherical demons: fast diffeomorphic landmark-free surface registration. IEEE Trans. Med. Imaging **29**(3), 650–668 (2010)
10. Robinson, E.C., Jbabdi, S., Glasser, M.F., Andersson, J., Burgess, G.C., Harms, M.P., Smith, S.M., Van Essen, D.C., Jenkinson, M.: MSM: a new flexible framework for multimodal surface matching. Neuroimage **100**, 414–426 (2014)
11. Rustamov, R.M.: Laplace-Beltrami eigenfunctions for deformation invariant shape representation. In: Proceedings of the Eurographics Symposium on Geometry Processing, pp. 225–233 (2007)
12. Lombaert, H., Sporring, J., Siddiqi, K.: Diffeomorphic spectral matching of cortical surfaces. In: Gee, J.C., Joshi, S., Pohl, K.M., Wells, W.M., Zöllei, L. (eds.) IPMI 2013. LNCS, vol. 7917, pp. 376–389. Springer, Heidelberg (2013). doi:10.1007/978-3-642-38868-2_32
13. Shi, Y., Lai, R., Wang, D.J., Pelletier, D., Mohr, D., Sicotte, N., Toga, A.W.: Metric optimization for surface analysis in the Laplace-Beltrami embedding space. IEEE Trans. Med. Imaging **33**(7), 1447–1463 (2014)
14. Essen, D.C.V., Smith, S.M., Barch, D.M., Behrens, T.E., Yacoub, E., Ugurbil, K.: The Wu-Minn human connectome project: an overview. NeuroImage **80**, 62–79 (2013)

15. Shi, Y., Lai, R., Morra, J., Dinov, I., Thompson, P., Toga, A.: Robust surface reconstruction via Laplace-Beltrami eigen-projection and boundary deformation. IEEE Trans. Med. Imaging **29**(12), 2009–2022 (2010)
16. Shen, L., Makedon, F.: Spherical mapping for processing of 3D closed surfaces. Image Vis. Comput. **24**(7), 743–761 (2006)
17. Tran, G., Shi, Y.: Fiber orientation and compartment parameter estimation from multi-shell diffusion imaging. IEEE Trans. Med. Imaging **34**(11), 2320–2332 (2015)